

Article

Magnetic Fe₂O₃–SiO₂–MeO₂–Pt (Me = Ti, Sn, Ce) as Catalysts for the Selective Hydrogenation of Cinnamaldehyde. Effect of the Nature of the Metal Oxide

Robinson Dinamarca ¹, Rodrigo Espinoza-González ², Cristian H. Campos ¹ and Gina Pecchi ^{1,3,*}

¹ Depto. Físico-Química, Facultad de Ciencias Químicas, Universidad de Concepción, Edmundo Larenas 129, Concepción 4070371, Chile; robidinamarca@udec.cl (R.D.); ccampos@udec.cl (C.H.C.)

² Department of Chemical Engineering, Biotechnology and Materials, FCFM, Universidad de Chile, Beauchef 851, Santiago 8370456, Chile; roespino@ing.uchile.cl

³ Millenium Nuclei on Catalytic Processes towards Sustainable Chemistry (CSC), Santiago 8340518, Chile

* Correspondence: gpecchi@udec.cl; Tel.: +56-41-220-3352

Received: 27 December 2018; Accepted: 23 January 2019; Published: 29 January 2019



Abstract: The type of metal oxide affects the activity and selectivity of Fe₂O₃–SiO₂–MeO₂–Pt (Me = Ti, Sn, Ce) catalysts on the hydrogenation of cinnamaldehyde. The double shell structure design is thought to protect the magnetic Fe₂O₃ cores, and also act as a platform for depositing a second shell of TiO₂, SnO₂ or CeO₂ metal oxide. To obtain a homogeneous metallic dispersion, the incorporation of 5 wt % of Pt was carried out over Fe₂O₃–SiO₂–MeO₂ (Me = Ti, Sn, Ce) structures modified with (3-aminopropyl)triethoxysilane by successive impregnation-reduction cycles. The full characterization by HR-TEM, STEM-EDX, XRD, N₂ adsorption isotherm at –196 °C, TPR-H₂ and VSM of the catalysts indicates that homogeneous *core-shell* structures with controlled nano-sized magnetic cores, multi-shells and metallic Pt were obtained. The nature of the metal oxide affects the Pt nanoparticle sizes where the mean Pt diameter is in the order: –TiO₂–Pt > –SnO₂–Pt > –CeO₂–Pt. Among the catalysts studied, –CeO₂–Pt had the best catalytic performance, reaching the maximum of conversion at 240 min. of reaction without producing hydrocinnamaldehyde (HCAL). It also showed a plot volcano type for the production of cinnamic alcohol (COL), with 3-phenyl-1-propanol (HCOL) as a main product. The –SnO₂–Pt catalyst showed a poor catalytic performance attributable to the Pt clusters' occlusion in the irregular surface of the –SnO₂. Finally, the –TiO₂–Pt catalyst showed a continuous production of COL with a 100% conversion and 65% selectivity at 600 min of reaction.

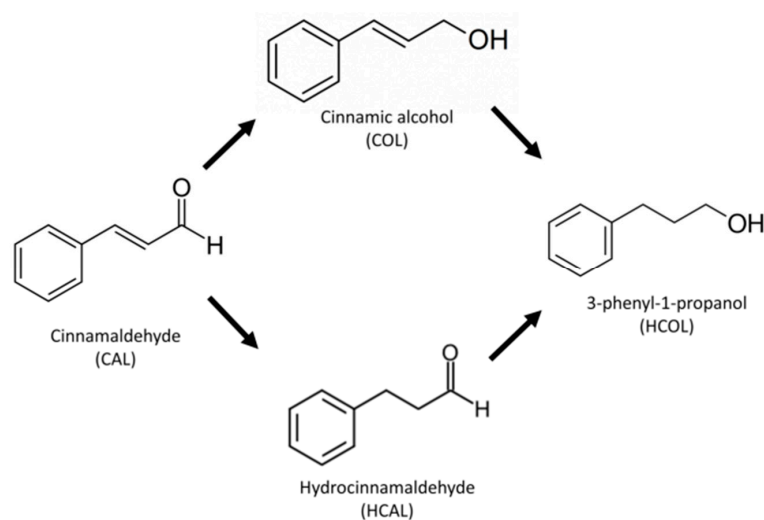
Keywords: nanocatalyst; core shell; hydrogenation

1. Introduction

Because of the versatility in composition and synthesis, materials with *core-shell* structure architecture have attracted particular attention in fields in which nanotechnology has a central role such as electronics [1], biomedicine [2], environmental remediation [3] and heterogeneous catalysis [4–6]. These materials in a nano- or micro-size structure produce a large surface-to-volume ratio, increasing the dominance of surface atoms and predominance of quantum effects, thereby improving their performance in various applications [7]. Efforts have been focused on the application of these materials in heterogeneous catalysts, specifically to increase their activity, operational stability and selectivity [8].

The selective catalytic hydrogenation of organic substrates containing a number of unsaturated functional groups is an important step in the industrial preparation of fine chemicals, increasing their relevancy for fundamental research in catalysis [9]. The heterogeneous selective hydrogenation,

using H_2 as reducing agent, of the carbonyl bonds in α,β -unsaturated aldehydes towards the formation of non-thermodynamically favored unsaturated alcohols, which are valuable intermediates in pharmaceutical, cosmetic, agrochemical and resin industries is still a challenge [10]. As a representative of α,β -unsaturated aldehydes, cinnamaldehyde (CAL) is principally used as a test molecule in the catalytic production of hydrocinnamaldehyde (HCAL), cinnamic alcohol (COL) and further hydrogenation to 3-phenyl-1-propanol (HCOL) [11], as shown in Scheme 1. In order to increase the selectivity of the COL production, different methods have been developed to improve the catalyst's performance, such as screening the transition metals for active phases, supporters and promoters [12].



Scheme 1. Cinnamaldehyde (CAL) hydrogenation pathways.

Among the transition metals, platinum (Pt) is the most-reported active phase in the hydrogenation of CAL. The selectivity of this active phase towards the formation of unsaturated alcohols has been attributed to the geometric and electronic defects of the metal [13] and can be improved by the incorporation of a second metal [14], a promoter [15], modification of the particle size [16] or by using a non-inert metal oxides in support [10,17] such as TiO_2 [11], SnO_2 [18], CeO_2 [19], ZnO [20], among others. Moreover, the well-known strong metal-support interaction (SMSI) effect promoted by partially reducible metal oxide [21–24] is observed in metal-supported catalysts submitted to a reducing atmosphere at temperatures above 300 °C. At this condition, the metal oxide partially covers the metallic phase, promoting C=O catalytic hydrogenation performance.

In the field of heterogeneous catalysis, the use of *core-shell* catalysts as single unit with different components has been previously reported [25–27]. For CAL hydrogenation, Song et al. has reported the use of a $Pt@CeO_2$ nanocatalyst achieving over 95% conversion with 87% selectivity to HCAL in 5 h under 1 atm H_2 pressure [28]. In the same way, Liu et al. used $MOF@Pt@MOF$ (MOF: Fe^{III} -based MIL-100) as a catalyst to produce COL at 96% selectivity and 95% of conversion of CAL in 4 h of reaction. However, the preparation process of MOF catalysts is relatively cumbersome, uneconomical and inapplicable in mass production.

One way to produce improved Pt-based catalysts is to employ a *core-shell* configuration, including a magnetic core isolated by a layer of oxide shell, which could act as support for Pt-metal nanoparticles (Pt NPs). The magnetic *core-shell* structure catalysts could provide the additional property of easy removal of the nanostructured catalyst by an external magnetic field [28]. The magnetic particles can be synthesized by different chemical methods; the polyol process is an effective sol-gel route for nano- and micro-particle synthesis with a controlled shape and size [29]. Moreover, is possible to modify the core materials to produce single-shell, multi-shell, or porous-shell structures to improve catalytic activity, selectivity and structural stability [3]. An alternative approach for the protection of magnetic cores is the use of the Stöber method to produce silica-coated shells on magnetic NPs via the facile

hydrolysis of tetraethyl orthosilicate (TEOS). It has been reported that uniform and robust silica shells have been formed by the complete hydrolysis of TEOS followed by the condensation of silicic acid, giving a network of tetrahedral SiO_4 units with shared vertices [30].

The surface physiochemical properties of small crystallites change dramatically at sizes lower than 5.0 nm, where the metal or metal oxide particles have low-coordinated surfaces, improving the catalytic activity [31]. The development of core-multi-shell nano-supports allows the shell characteristics to be modified in a controlled way in terms of the particle size, shape or crystallinity to improve their catalytic effect in terms of activity, selectivity and operational stability.

The aim of this work is to provide new magnetic multifunctional $\text{Fe}_2\text{O}_3\text{-SiO}_2\text{-MeO}_2\text{-Pt}$ (Me = Ti, Sn, Ce) nanomaterials as catalysts to be used in the selective hydrogenation of CAL. One of the most important steps to obtain the desired nanocatalyst structured microspheres is the coating process with TEOS for the formation of a silica shell as a protection layer for the magnetic core and a growth platform to provide for a homogeneous dispersal of a metal oxide shell on the $\text{Fe}_2\text{O}_3\text{-SiO}_2$ surface. The synthesis of the catalysts, while employing stepwise impregnation-reduction deposition, provides highly dispersed Pt catalysts in a *core-shell* structure. The effect of the nature of the metal oxide MeO_2 (Me = Ti, Sn, Ce) on well-stabilized magnetic core double shell structures in the selective hydrogenation of CAL was also described in this experiment.

2. Materials and Methods

2.1. Materials

Reagents were provided by Sigma[®] (Darmstadt, Germany) and Merck[®] (Darmstadt, Germany) Company and used without purification or treatment. These included iron chloride hydrate ($\text{FeCl}_3 \cdot 6\text{H}_2\text{O}$), ethylene glycol, sodium acetate, poly(vinylpyrrolidone) (PVP-K30), tetraethoxysilane (TEOS), ammonium hydroxide (NH₃ 28 wt %), ethanol, tetrabutyl orthotitanate (TBOT), Cerium nitrate (III) hexahydrate ($\text{Ce}(\text{NO}_3)_3 \cdot 6\text{H}_2\text{O}$), tin(IV) tert-butoxide (TTB), urea, D-xylose, toluene, (3-aminopropyl)trimethoxysilane (APTMS), K_2PtCl_6 and NaBH_4 .

2.2. $\text{Fe}_3\text{O}_4\text{-SiO}_2$ Structure

The $\text{Fe}_3\text{O}_4\text{-SiO}_2$ structures were synthesized starting from $\text{Fe}_3\text{O}_4\text{-NPs}$ coated with TEOS using the Stöber method in basic media [32]. The iron precursor ($\text{FeCl}_3 \cdot 6\text{H}_2\text{O}$) was dissolved in an ethylene glycol and PVP-K30 mixture, and sodium acetate was added as a nucleating agent under vigorous magnetic stirring for 5 h. The solution was transferred to a Teflon-autoclave reactor (Hydrion Scientific Instruments Company Ltd., Baltimore, MD, USA) and heated at 200 °C for 8 h to produce a homogeneous and stabilized $\text{Fe}_3\text{O}_4\text{-NPs}$ dispersion. Using magnetic separation, the dispersion was washed several times with an ethanol–water mixture before the coating procedure with $\text{Fe}_3\text{O}_4\text{-NPs}$ and TEOS as silica precursor. Then, 2 mL of TEOS was added drop-wise to 300 mg of $\text{Fe}_3\text{O}_4\text{-NPs}$ dispersed in a 180 mL ethanol, 60 mL water and 10 mL NH₃ mixture, while stirring with mechanical agitation for 6 h at room temperature. The solid was separated by magnetization, washed three times with an ethanol–water mixture and dried at 50 °C for 12 h to produce $\text{Fe}_3\text{O}_4\text{-SiO}_2$ nanostructures.

2.3. $\text{Fe}_2\text{O}_3\text{-SiO}_2$ and $\text{Fe}_2\text{O}_3\text{-SiO}_2\text{-MeO}_2$ (Me = Ti, Sn, Ce) Structures

The coating process with titanium and tin was carried out with a modified Stöber method [33], with 300 mg of $\text{Fe}_3\text{O}_4\text{-SiO}_2$ particles dispersed in 200 mL of ethanol and 1 mL ammonium solution, which was stirred for 1 h at 300 rpm under mechanical agitation. The condensation of the respective alkoxides was carried out by the addition drop-by-drop of 40 mL of ethanol with 5% by volume of the (Ti or Sn) alkoxide precursor to the dispersion and heating to 60 °C for 4 h. The coating process with Ce was carried out using a solvothermal methodology, as previously reported [34], with 300 mg of $\text{Fe}_3\text{O}_4\text{-SiO}_2$ particles dispersed in 300 mL of absolute ethanol sonicated for 30 min at room temperature. The addition drop-by-drop of 60 mL of an aqueous dissolution of 1.2 g urea, 6.0 g D-xylose and 1.0 g

cerium nitrate was carried out under mechanical agitation for 3 h. The mixture of the Ce precursor was transferred to a Teflon-autoclave reactor (Hydriion Scientific Instruments Company Ltd., Baltimore, MD, USA) and heated at 160 °C for 20 h. Finally, the Ti, Sn and Ce containing dispersions with Fe₃O₄-SiO₂-shells were washed three times with ethanol, dried overnight at 50 °C and calcined at 500 °C for 6 h. For comparison purposes, Fe₃O₄ NPs and Fe₃O₄-SiO₂ structures were also submitted to the calcination process at 500 °C for 6 h to produce Fe₂O₃ and Fe₂O₃-SiO₂ structures.

2.4. Fe₂O₃-SiO₂-MeO₂-Pt (Me = Ti, Sn, Ce) Catalysts

To better-control metallic dispersion, the incorporation of Pt was carried out on functionalized APTMS structures. The functionalized procedure that was carried out contacted the Fe₂O₃-SiO₂-MeO₂ (Me = Ti, Sn and Ce) structures with APTMS under reflux in toluene for 24 h, was washed with a 3:1 mixture of acetone:toluene and dried at 50 °C for 12 h. Then, the deposition of Pt-NPs was carried out using an aqueous dissolution of K₂PtCl₆ as a precursor and NaBH₄ as a reducing agent by successive impregnation-reduction steps until reaching a metallic loading of nominally ≈5 wt % Pt.

2.5. Characterization

The synthesis of the core-shell structures was studied by high-resolution transmission electron microscopy (HR-TEM) measurement. Morphology was examined using a FEI Tecnai G2 F20 S-Twin microscope (FEI, Hillsboro, OR, USA.), and the microanalysis was performed using a scanning transmission electron microscope (FEI, Hillsboro, OR, USA) and energy-dispersive X-ray spectroscopy (STEM-EDS) (FEI, Hillsboro, OR, USA). The total Pt and Fe content was determined by inductively coupled plasma-optical emission spectrometry (ICP-OES, Perkin Elmer optima 2100 DV ICP, (PerkinElmer, Waltham, MA, USA)) after dissolving the samples in 1:3 HNO₃:HCl mixtures and diluting them with doubly distilled water. The surface and pore size distributions by nitrogen adsorption isotherms were obtained using a Micromeritics apparatus Model ASAP 2010 at -196 °C (Norcross, GA, U.S.A). X-ray powder diffraction (XRD) pattern measurements were carried out with nickel-filtered CuK₁ radiation ($\lambda = 1.5418 \text{ \AA}$) collected on a Rigaku diffractometer (Rigaku, Tokyo, Japan) in the 2 θ range of 10°–80°. Temperature programmed reduction (TPR-H₂) profiles were obtained on Micromeritics TPR/TPD2900 equipment (Micromeritic, Norcross, GA, USA) provided with a thermal conductivity detector in 5% H₂/Ar flow at a rate of 40 mL·min⁻¹ from room temperature to 800 °C and a 5 °C·min⁻¹ heating rate. The surface charges of materials were determined by zeta potential in a Zetasizer NanoZS Marvern instrument (Malvern, Worcestershire, UK) with a provided electrode tray. Magnetic measurements were carried out at room temperature in a vibrating sample magnetometer (VSM) Lakeshore 7400 series (Lakeshore, New Orleans, LA, USA) with a maximum applied field of 20 kOe. The VSM had been previously calibrated with a pure nickel sphere.

2.6. Catalytic Activity

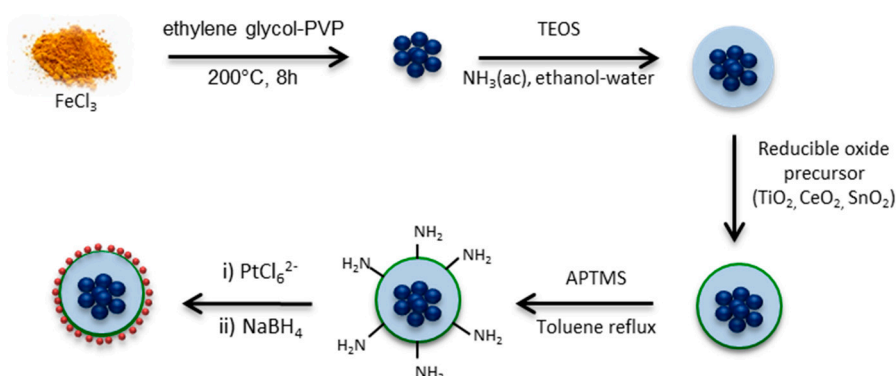
The catalytic activity evaluation of cinnamaldehyde was performed in a batch compact Parr[®] 5513 model reactor using 30 mg of catalyst weight and mechanical agitation up to 700 rpm. The reaction was performed at 100 °C, 2000 kPa of H₂, with a substrate/catalyst mole ratio equal to 600 in a volume of 30 mL of cyclohexane. The reaction was monitored by taking non-invasive samples periodically from the reaction mixture at different reaction times until total cinnamaldehyde conversion. The product quantifications were carried out using a gas chromatograph (Hewlett Packard HP-4890, Palo Alto, CA, USA) equipped with a capillary column (HP-5) and a flame ionization detector (FID).

3. Results and Discussion

3.1. Material Synthesis

The different steps carried out to produce well-defined Fe₂O₃-SiO₂-MeO₂-Pt (Me = Sn, Ce, Ti) catalysts were carefully designed and the main stages are shown in Scheme 2. Fe₃O₄ nanoparticles

were coated with TEOS to produce the starting core-SiO₂ structure. The first layer of silica between the iron species in the core and the further deposition of the metal MeO₂ (Me = Ti, Sn, Ce) oxide was designed to: (1) provide a regular, homogeneous and inert surface of SiO₂ for metal oxide deposition, (2) inhibit the effect of the metal oxides changing the magnetic behavior of the iron species in the core and (3) evaluate the effect of the metal oxide in the catalytic performance of Pt without the effect of the iron species present in the core. Furthermore, the surface of the Fe₂O₃-SiO₂-MeO₂ (Me = Ti, Sn, Ce) structures were functionalized with APTMS before the impregnation of Pt, to enhance the metallic dispersion and to carefully control the Pt particle size with successive impregnation-reduction cycles.



Scheme 2. Fe₂O₃-SiO₂-MeO₂-Pt (Me = Sn, Ce, Ti) synthesis pathways.

3.2. HR-TEM

The morphology and composition of the core-shell structures during the synthesis was followed by HR-TEM and the corresponding EDX analysis. The Fe₃O₄-NPs (Figure S1) used as cores corresponded to micro-spheres with regular shapes formed by nanosize Fe₃O₄ particles joined together in intimate contact, forming aggregates of Fe₃O₄-NPs with a mean diameter of ~230 nm. Single Fe₃O₄-NPs have been reported to have regular square shapes of 20–50 nm [35] as well as 180-nm colloidal nanocrystal clusters of Fe₃O₄, each one composed of many single magnetite crystallites of 10 nm [36]. The partial reduction process of the Fe(OH)_x species to Fe₃O₄ is likely carried out by a dehydration process promoted by the presence of ethylene glycol (reducing agent) at 200 °C during the solvothermal synthesis [29]. These Fe₃O₄ nanoparticles are then coated by a first SiO₂ shell by means of Stober's method, generating a structure Fe₃O₄-SiO₂ core-shell (Figure S2). This procedure allowed for the isolation of the magnetic core, thus providing a uniform surface to coat a second metal oxide shell. The mean diameter of ~320 nm for the Fe₃O₄-SiO₂ structures allows for an average estimated thickness of ~50 nm silica.

The HR-TEM micrographs of Fe₂O₃-SiO₂-MeO₂ (Me = Ti, Sn and Ce) structures are shown in Figure 1a–c. As it was said before, during the calcination step to produce the -MeO₂ oxides (Me = Ti, Sn and Ce), the Fe₃O₄ core was completely oxidized to γ-Fe₂O₃, in all of the samples, with almost no changes in the morphology. The Fe₂O₃-SiO₂-TiO₂ and Fe₂O₃-SiO₂-CeO₂ structures showed regular spherical shapes, which were indicative of a uniform metal oxide deposition on the surface of -SiO₂. The Fe₂O₃-SiO₂-SnO₂ displayed an irregular surface attributable to the presence of larger SnO₂ crystals. This trend is in agreement with the tin-based core-shell reported by Pang et al. [37], where the materials showed a non-defined coating after the deposition of SnO₂ on the titanium dioxide core surface.

In Figure 1d–f the corresponding STEM-EDS is shown, where the analysis was carried out in the zone marked in Figure 1a by a red diametral line indicating the scan of the chemical analysis. The Fe₂O₃-SiO₂-MeO₂ (Me = Ti, Sn, Ce) structures appeared in the EDS signals. The presence of the respective metal oxides at the edges of the structures is indicative of a well-coated thin double shell. The thickness of the metal oxide shell is estimated by the differences in the average particle diameter of Fe₂O₃-SiO₂ (Figure S2) in relation to Fe₂O₃-SiO₂-MeO₂ (Me = Ti, Sn, Ce) structures after counting more than 500 particles. The results obtained indicated a thickness of an average of ~20 nm for TiO₂, ~30 nm for

SnO_2 and ~ 15 nm for CeO_2 . The similar thicknesses for TiO_2 and SnO_2 materials were a consequence of the reported modified-Stöber method [33,38] that favored the interaction between the precursor alkoxide with silica and the smallest thickness of the CeO_2 coating materials added with the solvothermal method.

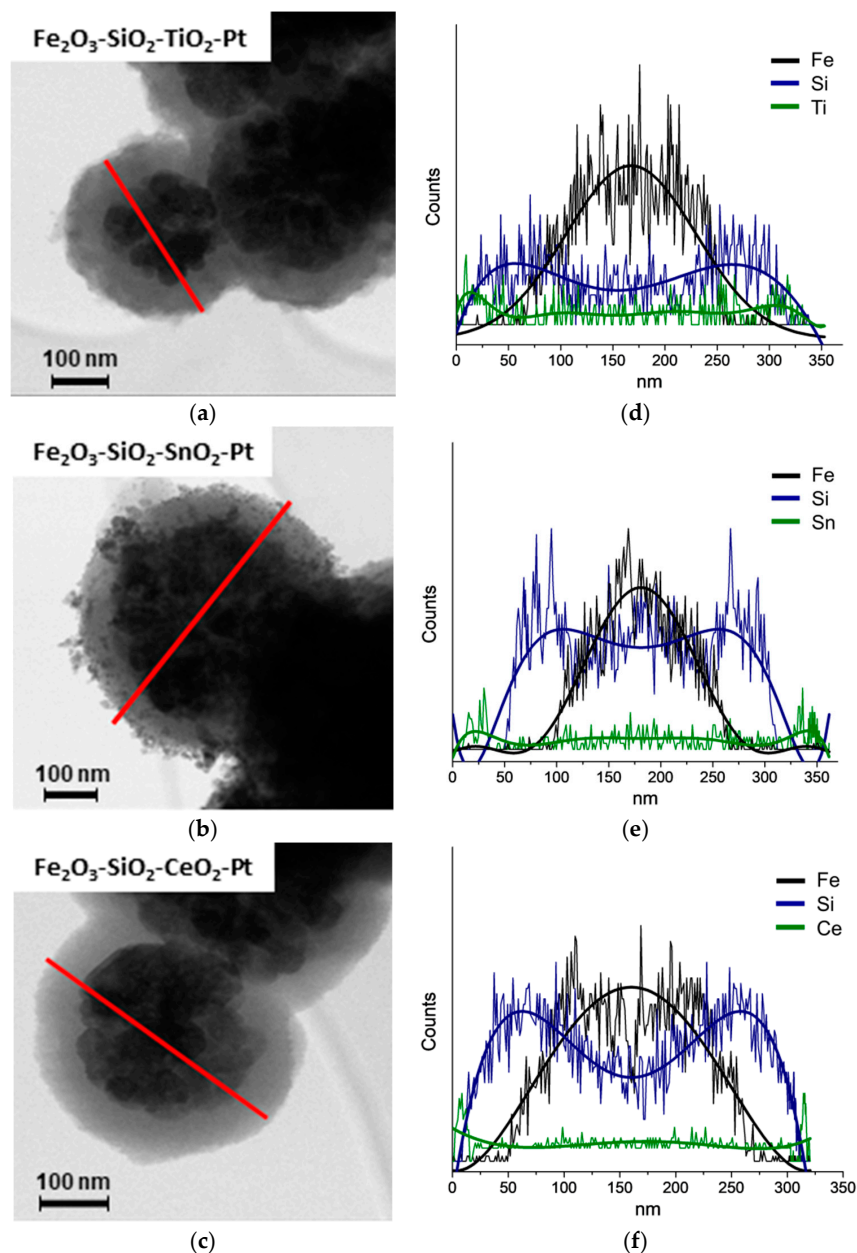


Figure 1. HR-TEM characterization for the synthesized *core-shell* materials. (a–c) HR-TEM micrographs and (d–f) STEM-EDX Fe (black), Si (blue), MeO_2 ; Me = Ti, Sn, Ce (green) for the $-\text{MeO}_2$ (Me = Ti, Sn, Ce) structures.

The HR-TEM micrographs of the $\text{Fe}_2\text{O}_3\text{-SiO}_2\text{-MeO}_2\text{-Pt}$ (Me = Ti, Sn, Ce) catalysts are shown in Figure 2. All of the catalysts showed narrow particle size distributions, and their diameter increased in the order of $\text{Fe}_2\text{O}_3\text{-SiO}_2\text{-CeO}_2\text{-Pt} < \text{Fe}_2\text{O}_3\text{-SiO}_2\text{-SnO}_2\text{-Pt} < \text{Fe}_2\text{O}_3\text{-SiO}_2\text{-TiO}_2\text{-Pt}$. This effect is mainly attributable to the nature of the metal oxide during the Pt deposition. In the catalyst syntheses, the $\text{Fe}_2\text{O}_3\text{-SiO}_2\text{-MeO}_2$ (Me = Ti, Sn, Ce) were contacted with the metal precursor (K_2PtCl_6) dissolved in aqueous solution to deposit the active phase on the shells (SiO_2 , TiO_2 , SnO_2 or CeO_2 modified with APTMS). The core-shell materials can accumulate PtCl_6^{2-} by a ligand-exchange process from the $-\text{NH}_2$ surface group and/or adsorb the metal precursor on the surface of the metal oxide by electrostatic

interaction. In Table 1, the zeta potential (ZP) measurements for the $\text{Fe}_2\text{O}_3\text{-SiO}_2\text{-MeO}_2$ (Me = Ti, Sn, Ce) aqueous dispersion are displayed. For all of the solids, ZP is a positive value, ascribable mainly to the presence of protonated amine groups from APTMS on the core-shell surface ($-\text{NH}_3^+$), because the pK_a of APTMS is 10.6 [39].

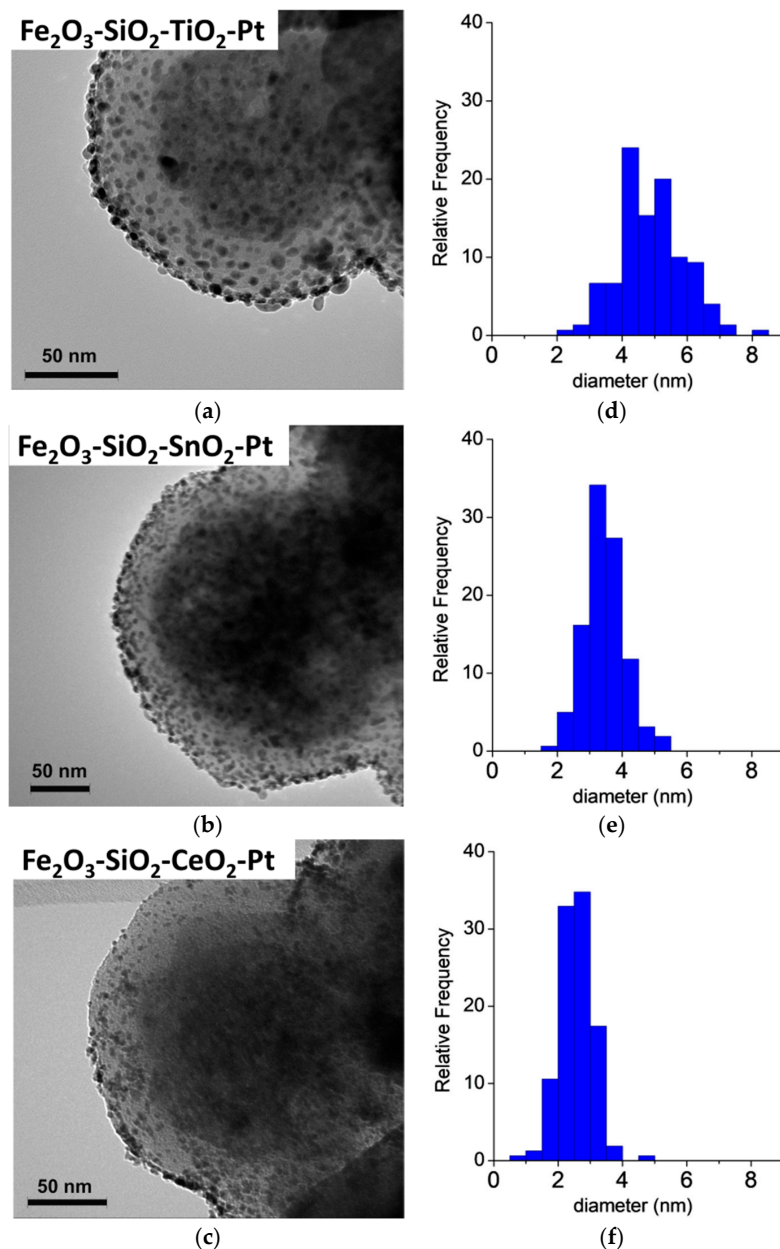


Figure 2. HR-TEM characterization for the synthesized Pt catalysts. (a–c) HR-TEM micrographs and (d–f) Pt particle size distribution.

Table 1. ICP results, Pt mean particle size by HRTEM and surface area of $\text{Fe}_2\text{O}_3\text{-SiO}_2\text{-Pt}$ and $\text{Fe}_2\text{O}_3\text{-SiO}_2\text{-MeO}_2\text{-Pt}$ (Me = Ti, Sn, Ce) catalysts.

Catalyst	ICP (%)		d_{Pt} (nm)	S_{BET} (m^2g^{-1})	ZP (mV)
	Fe	Pt			
$\text{Fe}_2\text{O}_3\text{-SiO}_2\text{-TiO}_2\text{-Pt}$	55	5.0	4.9 ± 1.0	10	23.7
$\text{Fe}_2\text{O}_3\text{-SiO}_2\text{-SnO}_2\text{-Pt}$	53	5.2	3.5 ± 0.7	14	37.3
$\text{Fe}_2\text{O}_3\text{-SiO}_2\text{-CeO}_2\text{-Pt}$	56	4.9	2.6 ± 0.5	11	19.0

Moreover, the metal oxides in the surface have different isoelectric point values (IEP): where $IEP_{TiO_2} = 5.9$ [40], $IEP_{SnO_2} = 6.4-7.3$ [41] and $IEP_{CeO_2} = 6.8-8.3$ [40]. The IEP is a reference for predicting the charge-dependent behavior of oxide minerals and their suspensions, in which IEP is a zero-point charge arising from the interaction of H^+ and OH^- with the solid and water [42]. In our case, the ZP at the pH of impregnation is positive, which enhances the metal precursors' electrical attraction from the dissolution to the stationary layer of fluid attached to the dispersed particle. During the reduction process with $NaBH_4$, the nucleation of $PtCl_6^{2-}$ to produce Pt NPs was enhanced in $Fe_2O_3-SiO_2-CeO_2$, mainly by the positive surface charge of $-CeO_2$ at pH = 6.5. In the case of $Fe_2O_3-SiO_2-SnO_2$, the IEP of $-SnO_2$ was close to the pH of the materials' dispersion (see Table 1) which is in line with an increase in the Pt NPs after the reduction process in comparison with the $-CeO_2$ -based core-shell. For the $Fe_2O_3-SiO_2-TiO_2$, the IEP was lower than for the other solids, which provided a negative surface charge on $-TiO_2$, which promoted an increase of Pt clusters during the reduction of Pt^{4+} to metallic Pt. Therefore, the large and homogeneous Pt metallic particle sizes can be attributed to the successive impregnation-reduction deposition. For comparison, we included HR-TEM micrograph for the $Fe_2O_3-SiO_2-TiO_2-Pt$, at 5 wt % Pt, prepared by the metal deposition in one step and a sequence of Pt depositions in multi-cycles for the $Fe_2O_3-SiO_2-TiO_2-Pt$ catalyst (see Materials and methods section). The $Fe_2O_3-SiO_2-TiO_2-Pt$ prepared in one step showed a mean Pt crystal size of 13.4 nm with a wide particle size distribution, which confirmed the irregular nucleation when this metal was loaded on the TiO_2 shell surface during the Pt deposition. Moreover, the multi-step metal precursor addition provided for, in the first cycle, the nucleation of smaller Pt NPs, which grew uniformly in every cycle as shown in the Supplementary Material (Figure S3).

3.3. ICP

The elemental composition of the $Fe_2O_3-SiO_2-MeO_2-Pt$ (Me = Ti, Sn, Ce) catalysts was determined by ICP spectroscopy and the results are in Table 1. A similar Fe content can be seen with almost no differences related to the metal oxide, which indicated a thin coverage of the double shell, as determined by EDX-Scan analysis. The Pt content approaches the nominal amount of 5 wt %, which was indicative of successful consecutive Pt impregnation-reduction cycles.

3.4. Specific Area

The adsorption-desorption nitrogen isotherms of the materials presented a type II IUPAC classification (Figure S4), which was indicative of non-porous structures. This result implied a non-textural modification during the sol-gel coating process not observed in the first shell of silica (see Table 1). It should be pointed out that, even though the materials had low surface areas, large platinum dispersions were observed in 5 wt % of Pt content catalysts, which supported the successful functionalization with APTMS and further Pt surface deposition impregnation-reduction cycles.

3.5. XRD

The XRD profiles of the Pt and non-Pt content structures are shown in Figure 3. Diffraction peaks can be seen, which indicated only the presence of maghemite $\gamma-Fe_2O_3$ (JCPDS 39-1356) as crystalline phases with an absence of Fe_3O_4 (JCPDS 65-3107) completely oxidized to Fe(III) (Figure S5). For the $Fe_2O_3-SiO_2-MeO_2$ (Me = Ti, Sn, Ce) structures, it can be seen that the coating process with the double shell of the metal oxide almost did not change the chemical composition of the crystalline Fe_2O_3 cores. There was only the apparition of segregated phases for the SnO_2 structures, and the lack of detection of crystalline structures for TiO_2 and CeO_2 indicated that they were present with a high degree of dispersion (the crystal size of the oxides was lower than 5.0 nm). It has been reported for $-TiO_2$ [4] that the nanocrystal size is controlled by the thickness of the TiO_2 coating process. On the other hand, for $-SnO_2$, the appearance of segregated phases of SnO_2 rutile with a tetragonal crystal system [43] has also been reported. Therefore, the appearance of only SnO_2 diffraction peaks is in agreement with the

HR-TEM results, regarding a more heterogeneous second coating process attributable to the behavior of the tin precursor to form polycrystalline SnO₂ nanoparticles [44].

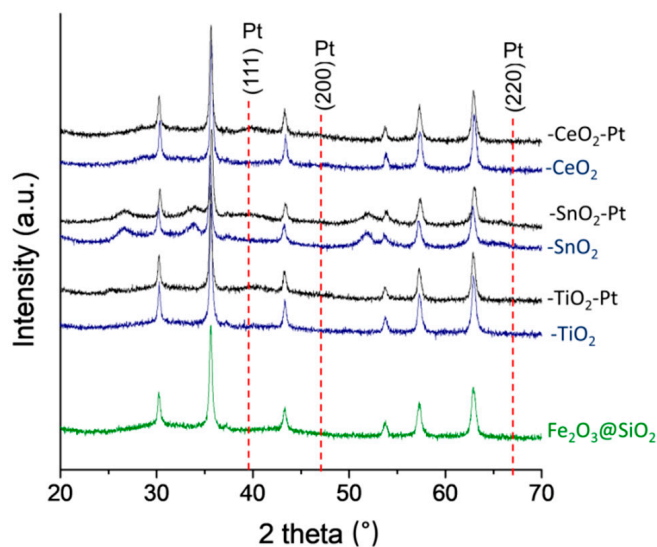


Figure 3. XRD patterns of Pt and non-Pt content of Fe₂O₃-SiO₂-MeO₂ (Me = Ti, Sn, Ce) materials.

With regard to the Pt-content catalysts, Fe₂O₃-SiO₂-MeO₂-Pt (Me = Ti, Sn, Ce) showed the same XRD profile as that of the pristine core-shell materials. This confirmed that the NaBH₄ used to perform the reduction of the metal precursor had no effect on the structure of the Fe₂O₃-SiO₂-MeO₂ (Me = Ti, Sn, Ce). However, the diffraction line at 39.6°, which corresponded to the metallic Pt(111) with a face-centred cubic structure, was too weak to be used to determine particle size in the case of Fe₂O₃-SiO₂-MeO₂-Pt (Me = Ti, Sn, Ce). Indeed, it is well recognized that the XRD technique is limited by the size of the particles. In this case, the size of the particle is less than 5 nm, which was in agreement with the HR-TEM characterization (see Table 1).

3.6. TPR-H₂

The TPR-H₂ profiles shown in Figure 4, corresponded to values normalized to per gram Fe to compare the intensity of the TCD signals independent of the more easily reducible FeO_x species and large iron content. In order to better see the reduction profiles of the Fe₂O₃-SiO₂-MeO₂-Pt (Me = Ti, Sn, Ce) catalysts in Figure 4, the profiles of Fe₂O₃-NPs is also shown. The additional experiment to produce Fe₂O₃-NPs was carried out on non-coated Fe₃O₄-NPs submitted to an oxidation treatment. The Fe₂O₃-NPs profiles indicated a first reduction step at 370 °C from hematite Fe₂O₃ to Fe₃O₄, followed by a broad reduction process started above 400 °C that can be deconvoluted into two peaks attributable to the Fe₃O₄→FeO and FeO→Fe steps [45]. The similarity of the TPR profiles for the Fe₂O₃-SiO₂-MeO₂-Pt; (Me = Ti, Sn, Ce) catalysts to the Fe₂O₃-NPs profile was a consequence of the larger content of Fe₂O₃ compared to the TiO₂, SnO₂ and CeO₂ oxides; the reduction process of TiO₂, SnO₂ and CeO₂ was masked by the reduction process of Fe₂O₃. Unfortunately, the broadening of the peaks of Figure 4 (that could not be deconvoluted into different reduction steps) are likely unassignable to a particular reduction process. The absence of a reduction step at low temperature indicates that the deposition of the platinum nanoparticles reduced with NaBH₄ at room temperature is the metallic state. To support this result, after the TPR of the -CeO₂-Pt system, an oxidation process in air at 300 °C for 1 h was carried out before a second TPR profile (Figure S6). The reduction step at 100 °C in the second TPR confirms the presence of metallic Pt in the -CeO₂-Pt catalyst.

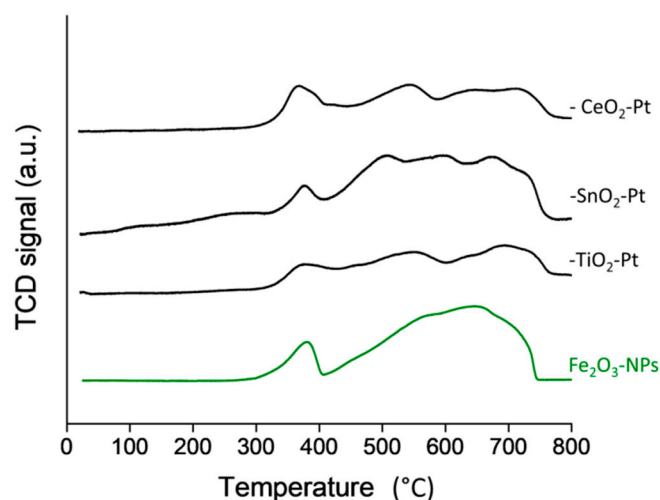


Figure 4. TPR-H₂ profile of Fe₂O₃-NPs and Fe₂O₃-SiO₂-MeO₂-Pt (Me = Ti, Sn, Ce) catalysts.

3.7. Magnetic Measurements

The magnetic hysteresis loops at room temperature of the materials scaled to g^{-1} of material are shown in Figure 5. The Fe₂O₃-SiO₂-MeO₂-Pt (Me = Ti, Sn, Ce) structures display a ferromagnetic behavior with a magnetic saturation of $\sim 40 \text{ emu} \cdot \mu\text{g}^{-1}$. The remanence and coercivity properties of the hysteresis loop (inset of Figure 5) was attributable to the grain size of the core and limited for the silica coating process [2]. An increase in the coercivity of nanostructures has been reported due to an increase in both magnetocrystalline and shape anisotropy, which exert influence on the nanostructures' magnetic properties [46]. Due to the metal oxide content, structures did not show a change in the shape of the hysteresis loop, which confirmed that the magnetic properties of the material were confined to the core structure. The observed remanence and coercivity values allowed for the easy separation of the prepared catalysts from the reaction medium using external magnetic fields [32]. This phenomenon is appreciated because it is possible to separate the solid from the middle of the reaction in 30 s after putting it in contact with a magnet (Figure 5).

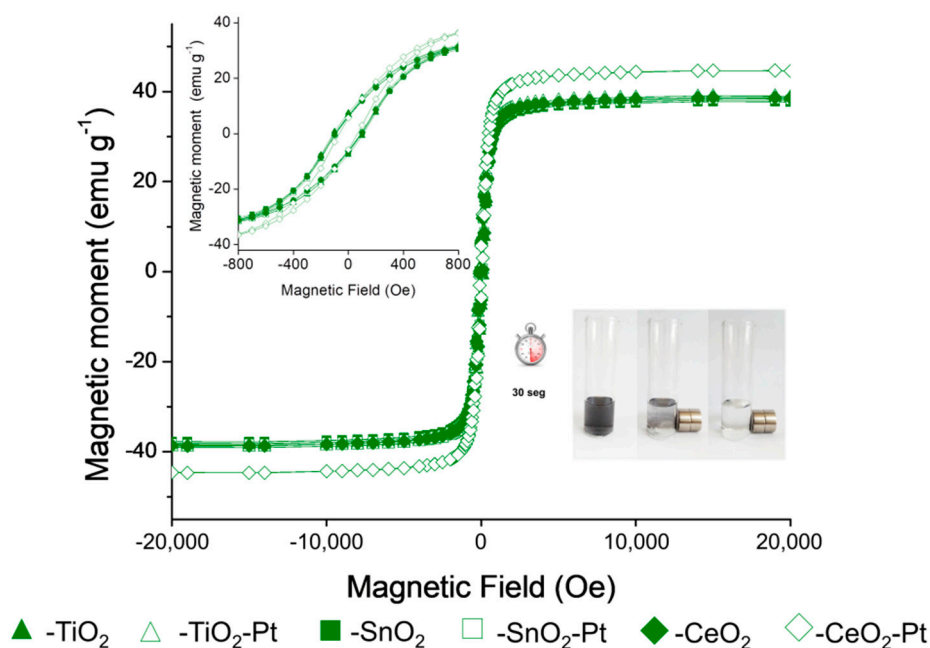


Figure 5. Magnetic measurements of Fe₂O₃-SiO₂-MeO₂ and Fe₂O₃-SiO₂-MeO₂-Pt (Me = Ti, Sn, Ce) materials. Inset zoom of the hysteresis loop.

3.8. Catalytic Performance

The selective catalytic hydrogenation of CAL to COL is an ambitious challenge and aspects such as the nanometric size (1–10 nm) of the active sites, surface structure, metal-support interactions and electronic effects become more important in achieving it [47], and these factors should be considered for describing a catalyst's performance. To increase the selectivity towards the high-value-added COL, the nature of the shell as support for Pt NPs was studied as part of this work. The CAL conversion curves with reaction time for the $\text{Fe}_2\text{O}_3\text{-SiO}_2\text{-MeO}_2\text{-Pt}$ (Me = Ti, Sn, Ce) catalysts are shown in Figure 6a, and to better illustrate the effect of the metal oxide type on the conversion levels, Figure 6b shows the successful fit of the experimental data with a pseudo 1st order reaction.

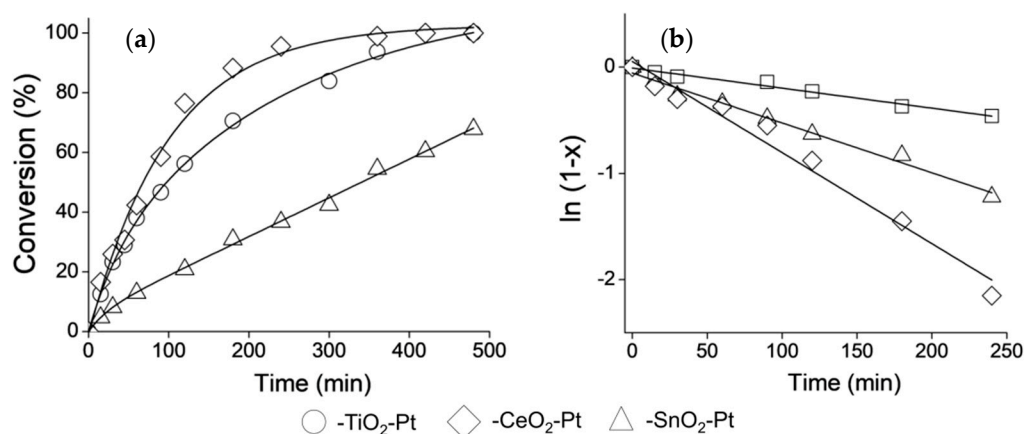


Figure 6. Catalytic evaluation of $\text{Fe}_2\text{O}_3\text{-SiO}_2\text{-MeO}_2\text{-Pt}$ (Me = Ti, Sn, Ce) in CAL Hydrogenation. (a) Conversion curves and (b) Pseudo-first order kinetic model adjustment.

The calculated pseudo-1st-order reaction rate constants, the initial reaction rates, maximum conversions at 500 min. and selectivity are shown in Table 2. More than 99% conversion and 67% COL production selectivity were obtained at 300 min. when $\text{Fe}_2\text{O}_3\text{-SiO}_2\text{-CeO}_2\text{-Pt}$ was used as catalyst, while the $\text{Fe}_2\text{O}_3\text{-SiO}_2\text{-TiO}_2\text{-Pt}$ system only reached 78% conversion and 65% selectivity for COL during the same time of reaction. In contrast, the conversion decreased to 40% and the selectivity value lowered to 50% for the $\text{Fe}_2\text{O}_3\text{-SiO}_2\text{-SnO}_2\text{-Pt}$ system.

Table 2. Global pseudo-first order constant (k_{global}), initial reaction rate (r_0) and selectivity at 60% of conversion level of the $\text{Fe}_2\text{O}_3\text{-SiO}_2\text{-MeO}_2\text{-Pt}$ (Me = Ti, Sn, Ce) catalysts.

Catalyst	k_{global} ($\text{min}^{-1}\cdot\text{g}^{-1}$)	r_0 ($\text{mmol}\cdot\text{L}^{-1}\cdot\text{h}^{-1}$)	Selectivity (%)		
			COL	HCOL	HCAL
$\text{Fe}_2\text{O}_3\text{-SiO}_2\text{-TiO}_2\text{-Pt}$	0.20	47	67	13	20
$\text{Fe}_2\text{O}_3\text{-SiO}_2\text{-SnO}_2\text{-Pt}$	0.073	17	48	6	46
$\text{Fe}_2\text{O}_3\text{-SiO}_2\text{-CeO}_2\text{-Pt}$	0.41	97	65	22	12

For the selective hydrogenation of CAL, it is well-documented that the particle size of active metal species can exert vital impacts on their catalytic performance [47]. Generally, the decrease in the metal particle size leads to both the increased activity and the decreased COL selectivity. This is due to more active sites on small-sized metal particles that have less-coordinated surface sites and the higher adsorption strength of C=C bonds versus C=O bonds. In the other way, the use of -TiO_2 , -SnO_2 and -CeO_2 as shells was designed with the aim to increase the selectivity towards COL product, due to they have been reported as non-inert supports which could provide SMSI effect even at room temperature [23].

In the present work, although the sizes of Pt NPs were different (see Table 1), $\text{Fe}_2\text{O}_3\text{-SiO}_2\text{-CeO}_2\text{-Pt}$ had the best catalytic performance. Due to the different sizes of Pt particles, there was a size dependence of hydrogenation activity among these catalysts. However, the pseudo-1st-order reaction rate constant follows the trend $k_{\text{-CeO}_2} > k_{\text{-TiO}_2} \gg k_{\text{-SnO}_2}$, which is different from the trend for the Pt mean particle size, where $\text{-CeO}_2\text{-Pt} > \text{-SnO}_2\text{-Pt} > \text{-TiO}_2\text{-Pt}$. This behavior can be explained by the nature of the -SnO_2 shell in the $\text{Fe}_2\text{O}_3\text{-SiO}_2\text{-SnO}_2\text{-Pt}$. The -SnO_2 shell possess an irregular surface with evident formations of SnO_2 clusters with particle sizes larger than the Pt NPs, as was demonstrated by HR-TEM and XRD characterization. Despite the production of Pt NPs with a mean size of 3.5 nm (see Table 1), the crystals were almost randomly dispersed in the -SnO_2 interstices as hetero-aggregates, which could block the active sites, thereby decreasing the conversion levels. In relation to the results for $k_{\text{-CeO}_2} > k_{\text{-TiO}_2}$, the ratio of the pseudo-1st-order reaction rate constant was $k_{\text{-CeO}_2}:k_{\text{-TiO}_2} = 2.2:1$, which is in agreement with the differences in the Pt particle sizes, where their size ratio in $\text{-TiO}_2\text{-Pt}:\text{-CeO}_2\text{-Pt}$ was 1.9:1.

The selectivity was the most interesting result; $\text{Fe}_2\text{O}_3\text{-SiO}_2\text{-TiO}_2\text{-Pt}$ catalysts showed a high selectivity to the desired product during the entire reaction course. For a better understanding, Figure 7 shows the product distribution as a function of time for all of the catalysts until 500 min. of reaction. The decrease of the catalyst selectivity in the $\text{Fe}_2\text{O}_3\text{-SiO}_2\text{-CeO}_2\text{-Pt}$ system is in line with work reported by Wei et al in the selective hydrogenation of CAL over a Pt/CeO₂ catalyst [19]. The $\text{Fe}_2\text{O}_3\text{-SiO}_2\text{-CeO}_2\text{-Pt}$ catalyst displayed a sharp decrease in the CAL concentration in the initial reaction period. The CAL concentration reached near total consumption after 240 min. Meanwhile, the COL concentration increased gradually in the total reaction period of 120 min. However, the production of HCOL also increased rapidly after 120 min. of reaction, reflecting a thermodynamically favorable hydrogenation of the C=C bond. Despite of the presence of CeO₂ which could promote the SMSI effect at the reaction temperature, as was observed at lower conversion level, the low mean Pt crystal size enhance the over-hydrogenation of both COL and HCAL producing mainly HCOL at high conversion level.

In the selective hydrogenation of CAL, it has been reported that the adsorption of the C=O bond towards the formation of the unsaturated alcohol is favored on larger metallic particle sizes [47–50]. However, for the $\text{Fe}_2\text{O}_3\text{-SiO}_2\text{-TiO}_2\text{-Pt}$ catalyst, a continuous increase in the COL formation can be seen with no further second hydrogenation step. We propose that the chemical properties of the TiO₂ loading shell could generate an active site favoring the adsorption through the C=O, which inhibited the coplanar adsorption of CAL by both Pt crystal size and SMSI effect. Moreover, in the $\text{Fe}_2\text{O}_3\text{-SiO}_2\text{-TiO}_2\text{-Pt}$ catalyst, the total hydrogenation product (HCOL) results from the HCAL hydrogenation with non-consumption of COL at 180 min which are in agreement with the preferred C=O adsorption on the catalyst surface.

Finally, for the $\text{Fe}_2\text{O}_3\text{-SiO}_2\text{-SnO}_2\text{-Pt}$ catalyst, the competitive adsorption of the substrate by the SnO₂ crystallites and the homogeneous and narrow Pt particle sizes produced HCAL and COL in almost the same proportion. Moreover, although CAL hydrogenation does not require acid sites, in the smallest Pt nanoparticles, the Lewis acid properties of SnO₂ influenced the reaction rate and the selectivity of the process by modifying the adsorptive properties of Pt because of surface electron density [50]. Therefore, the observed selectivity results can be attributed to surface modification and metal-support interactions as well as a decrease in the Pt particle size [47].

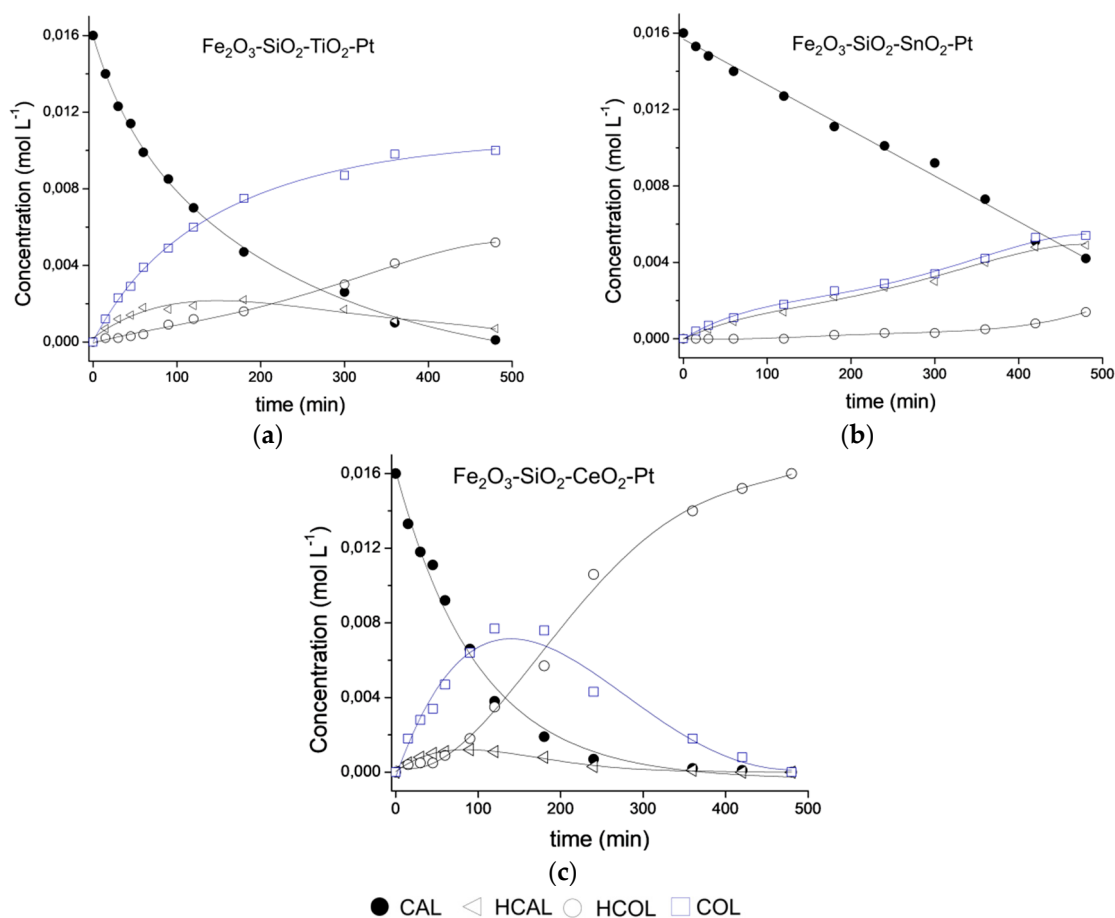


Figure 7. Product distribution during CAL hydrogenation on (a) Fe₂O₃-SiO₂-TiO₂-Pt, (b) Fe₂O₃-SiO₂-SnO₂-Pt and (c) Fe₂O₃-SiO₂-CeO₂-Pt catalysts.

4. Conclusions

Fe₂O₃-SiO₂-MeO₂-Pt (Me = Ti, Sn, Ce) magnetic *core-shell* catalysts were successfully prepared. The use of -SiO₂ shells provided a protected magnetic core, and its structure ensured the deposition of a second metal oxide shell, which preserved the shape of the Fe₂O₃-SiO₂ structure. The Pt metal nanoparticles deposited in continuous cycles provided support to the catalyst with a homogeneous metal dispersion on the -MeO₂ surface (Me = Ce, Sn, Ti). In addition, the nature of the metal oxide affected the Pt mean particle diameters in the order of -TiO₂-Pt > -SnO₂-Pt > -CeO₂-Pt. This trend was attributed to the IEP of the solids, which affected the interaction of metal precursors with the surfaces of the metal oxide shells. Consequently, the catalytic activity showed the trend of -CeO₂-Pt > -TiO₂-Pt > -SnO₂-Pt, which is line with the physicochemical properties of the core-shell catalysts. In the case of -CeO₂-Pt, an excellent activity and a continuous decrease in the production of COL was attributed to the Pt mean particle size (2.6 nm), which enhanced the consumption of both CAL and COL to produce of HCOL at a higher CAL conversion. In the opposite direction, -SnO₂-Pt showed a minor activity in comparison with the other catalysts, mainly attributed to the irregular SnO₂ shell surface, which allowed for the formation of Pt nanoparticles inside the SnO₂ crystals, thereby blocking the active phase, which decreased the catalytic performance. The large stability towards the production of the unsaturated cinnamic alcohol of the -TiO₂-Pt catalyst is attributed to particle size (4.9 nm) and the chemical properties of the TiO₂ loading shell favoring the adsorption of CAL by the C=O bond, inhibiting the coplanar adsorption of CAL to produce HCAL and/or HCOL. This study suggests both Pt nanoparticles size and SMSI effects have resulted beneficial in selective hydrogenation of CAL to produce COL as the main product.

Supplementary Materials: The following are available online at <http://www.mdpi.com/1996-1944/12/3/413/s1>, Figure S1: Micrograph of Fe₃O₄ nanoparticles, Figure S2: Micrograph of Fe₃O₄-SiO₂ core-shell material, Figure S3: Micrograph of Fe₂O₃-SiO₂-TiO₂-5%Pt one-step core-shell material, Figure S4: N₂ adsorption desorption Isotherm, Figure S5: XRD pattern for Fe₃O₄ and γ -Fe₂O₃ nanoparticles, Figure S6: TPR-1 and TPR-2 of Fe₃O₄-SiO₂-CeO₂-Pt.

Author Contributions: R.D. performed the synthesis; R.E.-G. performed the HRTEM characterization. C.H.C. performed the design of the synthesis, characterization and catalytic result analysis and review and edit the manuscript; G.P. performed the characterization and catalytic result analysis and wrote the manuscript.

Funding: This research was funded by Fondecyt 1170083 (G.P.), Fondecyt initiation 11170095 (C.H.C.) and Millennium Nucleus MULTIMAT—ICM/MINECON (R.E.-G.).

Acknowledgments: The authors thank to Gorka Salas of the Instituto Madrileño de Estudios Avanzados en Nanociencia, IMDEA, Spain for their Magnetic Measurements and CONICYT Grant 21150092 (R.D.).

Conflicts of Interest: The authors declare no conflict of interest.

References

1. Lee, C.H.; Ma, Y.; Jang, K.-I.; Banks, A.; Pan, T.; Feng, X.; Kim, J.S.; Kang, D.; Raj, M.S.; McGrane, B.L.; et al. Soft Core/Shell Packages for Stretchable Electronics. *Adv. Funct. Mater.* **2015**, *25*, 3698–3704. [[CrossRef](#)]
2. Akbarzadeh, A.; Samiei, M.; Davaran, S. Magnetic nanoparticles: Preparation, physical properties, and applications in biomedicine. *Nanoscale Res. Lett.* **2012**, *7*, 144. [[CrossRef](#)] [[PubMed](#)]
3. Mondal, K.; Sharma, A. Recent advances in the synthesis and application of photocatalytic metal–metal oxide core–shell nanoparticles for environmental remediation and their recycling process. *RSC Adv.* **2016**, *6*, 83589–83612. [[CrossRef](#)]
4. Ye, M.; Zhang, Q.; Hu, Y.; Ge, J.; Lu, Z.; He, L.; Chen, Z.; Yin, Y. Magnetically Recoverable Core–Shell Nanocomposites with Enhanced Photocatalytic Activity. *Chem. Eur. J.* **2010**, *16*, 6243–6250. [[CrossRef](#)] [[PubMed](#)]
5. Joo, S.H.; Park, J.Y.; Tsung, C.-K.; Yamada, Y.; Yang, P.; Somorjai, G.A. Thermally stable Pt/mesoporous silica core–shell nanocatalysts for high-temperature reactions. *Nat. Mater.* **2008**, *8*, 126. [[CrossRef](#)] [[PubMed](#)]
6. Ikeda, S.; Ishino, S.; Harada, T.; Okamoto, N.; Sakata, T.; Mori, H.; Kuwabata, S.; Torimoto, T.; Matsumura, M. Ligand-Free Platinum Nanoparticles Encapsulated in a Hollow Porous Carbon Shell as a Highly Active Heterogeneous Hydrogenation Catalyst. *Angew. Chem.* **2006**, *118*, 7221–7224. [[CrossRef](#)]
7. Ghosh Chaudhuri, R.; Paria, S. Core/Shell Nanoparticles: Classes, Properties, Synthesis Mechanisms, Characterization, and Applications. *Chem. Rev.* **2012**, *112*, 2373–2433. [[CrossRef](#)] [[PubMed](#)]
8. Fernandes, C.I.; Capelli, S.C.; Vaz, P.D.; Nunes, C.D. Highly selective and recyclable MoO₃ nanoparticles in epoxidation catalysis. *Appl. Catal. A* **2015**, *504*, 344–350. [[CrossRef](#)]
9. Claus, P. Selective hydrogenation of α,β -unsaturated aldehydes and other C=O and C=C bonds containing compounds. *Top. Catal.* **1998**, *5*, 51–62. [[CrossRef](#)]
10. Piqueras, C.M.; Puccia, V.; Vega, D.A.; Volpe, M.A. Selective hydrogenation of cinnamaldehyde in supercritical CO₂ over Me–CeO₂ (Me = Cu, Pt, Au): Insight of the role of Me–Ce interaction. *Appl. Catal. B* **2016**, *185*, 265–271. [[CrossRef](#)]
11. Wu, Q.; Zhang, C.; Zhang, B.; Li, X.; Ying, Z.; Liu, T.; Lin, W.; Yu, Y.; Cheng, H.; Zhao, F. Highly selective Pt/ordered mesoporous TiO₂–SiO₂ catalysts for hydrogenation of cinnamaldehyde: The promoting role of Ti²⁺. *J. Colloid Interface Sci.* **2016**, *463*, 75–82. [[CrossRef](#)] [[PubMed](#)]
12. Rong, Z.; Sun, Z.; Wang, Y.; Lv, J.; Wang, Y. Selective Hydrogenation of Cinnamaldehyde to Cinnamyl Alcohol over Graphene Supported Pt–Co Bimetallic Catalysts. *Catal. Lett.* **2014**, *144*, 980–986. [[CrossRef](#)]
13. Laref, S.; Delbecq, F.; Loffreda, D. Theoretical elucidation of the selectivity changes for the hydrogenation of unsaturated aldehydes on Pt(111). *J. Catal.* **2009**, *265*, 35–42. [[CrossRef](#)]
14. Zheng, Q.; Wang, D.; Yuan, F.; Han, Q.; Dong, Y.; Liu, Y.; Niu, X.; Zhu, Y. An Effective Co-promoted Platinum of Co–Pt/SBA-15 Catalyst for Selective Hydrogenation of Cinnamaldehyde to Cinnamyl Alcohol. *Catal. Lett.* **2016**, *146*, 1535–1543. [[CrossRef](#)]
15. Hsu, C.-Y.; Chiu, T.-C.; Shih, M.-H.; Tsai, W.-J.; Chen, W.-Y.; Lin, C.-H. Effect of Electron Density of Pt Catalysts Supported on Alkali Titanate Nanotubes in Cinnamaldehyde Hydrogenation. *J. Phys. Chem. C* **2010**, *114*, 4502–4510. [[CrossRef](#)]

16. Plomp, A.J.; Vuori, H.; Krause, A.O.I.; de Jong, K.P.; Bitter, J.H. Particle size effects for carbon nanofiber supported platinum and ruthenium catalysts for the selective hydrogenation of cinnamaldehyde. *Appl. Catal. A* **2008**, *351*, 9–15. [[CrossRef](#)]
17. Helali, Z.; Jedidi, A.; Syzgantseva, O.A.; Calatayud, M.; Minot, C. Scaling reducibility of metal oxides. *Theor. Chem. Acc.* **2017**, *136*, 100. [[CrossRef](#)]
18. Dai, L.-X.; Zhu, W.; Lin, M.; Zhang, Z.-P.; Gu, J.; Wang, Y.-H.; Zhang, Y.-W. Self-supported composites of thin Pt–Sn crosslinked nanowires for the highly chemoselective hydrogenation of cinnamaldehyde under ambient conditions. *Inorg. Chem. Front.* **2015**, *2*, 949–956. [[CrossRef](#)]
19. Wei, S.; Zhao, Y.; Fan, G.; Yang, L.; Li, F. Structure-dependent selective hydrogenation of cinnamaldehyde over high-surface-area CeO₂–ZrO₂ composites supported Pt nanoparticles. *Chem. Eng. J.* **2017**, *322*, 234–245. [[CrossRef](#)]
20. Fujita, S.-I.; Mitani, H.; Zhang, C.; Li, K.; Zhao, F.; Arai, M. Pd and Pd Zn supported on ZnO as catalysts for the hydrogenation of cinnamaldehyde to hydrocinnamyl alcohol. *Mol. Catal.* **2017**, *442*, 12–19. [[CrossRef](#)]
21. Tauster, S.J.; Fung, S.C.; Baker, R.T.K.; Horsley, J.A. Strong Interactions in Supported-Metal Catalysts. *Science* **1981**, *211*, 1121–1125. [[CrossRef](#)] [[PubMed](#)]
22. Resasco, D.E.; Weber, R.S.; Sakellson, S.; McMillan, M.; Haller, G.L. X-ray absorption near-edge structure evidence for direct metal-metal bonding and electron transfer in reduced rhodium/titania catalysts. *J. Phys. Chem.* **1988**, *92*, 189–193. [[CrossRef](#)]
23. Rui, Z.; Chen, L.; Chen, H.; Ji, H. Strong Metal-Support Interaction in Pt/TiO₂ Induced by Mild HCHO and NaBH₄ Solution Reduction and Its Effect on Catalytic Toluene Combustion. *Ind. Eng. Chem. Res.* **2014**, *53*, 15879–15888. [[CrossRef](#)]
24. Zhao, E.W.; Zheng, H.; Ludden, K.; Xin, Y.; Hagelin-Weaver, H.E.; Bowers, C.R. Strong Metal-Support Interactions Enhance the Pairwise Selectivity of Parahydrogen Addition over Ir/TiO₂. *ACS Catal.* **2016**, *6*, 974–978. [[CrossRef](#)]
25. Li, Z.; Li, M.; Bian, Z.; Kathiraser, Y.; Kawi, S. Design of highly stable and selective core/yolk-shell nanocatalysts—A review. *Appl. Catal. B* **2016**, *188*, 324–341. [[CrossRef](#)]
26. Zhang, J.; Medlin, J.W. Catalyst design using an inverse strategy: From mechanistic studies on inverted model catalysts to applications of oxide-coated metal nanoparticles. *Surf. Sci. Rep.* **2018**, *73*, 117–152. [[CrossRef](#)]
27. Hanske, C.; Sanz-Ortiz, M.N.; Liz-Marzán, L.M. Silica-Coated Plasmonic Metal Nanoparticles in Action. *Adv. Mater.* **2018**, *30*, 1707003. [[CrossRef](#)]
28. Song, S.; Liu, X.; Li, J.; Pan, J.; Wang, F.; Xing, Y.; Wang, X.; Liu, X.; Zhang, H. Confining the Nucleation of Pt to In Situ Form (Pt-Enriched Cage)@CeO₂ Core@Shell Nanostructure as Excellent Catalysts for Hydrogenation Reactions. *Adv. Mater.* **2017**, *29*, 1700495. [[CrossRef](#)]
29. Zhang, W.; Shen, F.; Hong, R. Solvothermal synthesis of magnetic Fe₃O₄ microparticles via self-assembly of Fe₃O₄ nanoparticles. *Particuology* **2011**, *9*, 179–186. [[CrossRef](#)]
30. Wong, Y.J.; Zhu, L.; Teo, W.S.; Tan, Y.W.; Yang, Y.; Wang, C.; Chen, H. Revisiting the Stöber Method: Inhomogeneity in Silica Shells. *J. Am. Chem. Soc.* **2011**, *133*, 11422–11425. [[CrossRef](#)] [[PubMed](#)]
31. Rioux, R.M.; Song, H.; Grass, M.; Habas, S.; Niesz, K.; Hoefelmeyer, J.D.; Yang, P.; Somorjai, G.A. Monodisperse platinum nanoparticles of well-defined shape: Synthesis, characterization, catalytic properties and future prospects. *Top. Catal.* **2006**, *39*, 167–174. [[CrossRef](#)]
32. Long, Y.; Liang, K.; Niu, J.; Yuan, B.; Ma, J. Pt NPs immobilized on core-shell magnetite microparticles: Novel and highly efficient catalysts for the selective aerobic oxidation of ethanol and glycerol in water. *Dalton Trans.* **2015**, *44*, 8660–8668. [[CrossRef](#)] [[PubMed](#)]
33. Dong, W.; Zhu, Y.; Huang, H.; Jiang, L.; Zhu, H.; Li, C.; Chen, B.; Shi, Z.; Wang, G. A performance study of enhanced visible-light-driven photocatalysis and magnetical protein separation of multifunctional yolk-shell nanostructures. *J. Mater. Chem. A* **2013**, *1*, 10030–10036. [[CrossRef](#)]
34. Li, S.; Cai, J.; Wu, X.; Liu, B.; Chen, Q.; Li, Y.; Zheng, F. TiO₂@Pt@CeO₂ nanocomposite as a bifunctional catalyst for enhancing photo-reduction of Cr(VI) and photo-oxidation of benzyl alcohol. *J. Hazard. Mater.* **2018**, *346*, 52–61. [[CrossRef](#)]
35. Channei, D.; Inceesungvorn, B.; Wetchakun, N.; Phanichphant, S. Synthesis of Fe₃O₄/SiO₂/CeO₂ Core@Shell Magnetic and Their Application as Photocatalyst. *J. Nanosci. Nanotechnol.* **2014**, *14*, 7756–7762. [[CrossRef](#)] [[PubMed](#)]

36. Ge, J.; Hu, Y.; Biasini, M.; Beyermann, W.P.; Yin, Y. Superparamagnetic Magnetite Colloidal Nanocrystal Clusters. *Angew. Chem. Int. Ed.* **2007**, *46*, 4342–4345. [[CrossRef](#)] [[PubMed](#)]
37. Pang, A.; Sun, X.; Ruan, H.; Li, Y.; Dai, S.; Wei, M. Highly efficient dye-sensitized solar cells composed of TiO₂@SnO₂ core-shell microspheres. *Nano Energy* **2014**, *5*, 82–90. [[CrossRef](#)]
38. Kar, A.; Patra, A. Recent development of core-shell SnO₂ nanostructures and their potential applications. *J. Mater. Chem. C* **2014**, *2*, 6706–6722. [[CrossRef](#)]
39. Niu, D.; Li, Y.; Qiao, X.; Li, L.; Zhao, W.; Chen, H.; Zhao, Q.; Ma, Z.; Shi, J. A facile approach to fabricate functionalized superparamagnetic copolymer-silica nanocomposite spheres. *Chem. Commun.* **2008**, 4463–4465. [[CrossRef](#)]
40. Berg, J.M.; Romoser, A.; Banerjee, N.; Zebda, R.; Sayes, C.M. The relationship between pH and zeta potential of ~ 30 nm metal oxide nanoparticle suspensions relevant to in vitro toxicological evaluations. *Nanotoxicology* **2009**, *3*, 276–283. [[CrossRef](#)]
41. Maurya, S.; Shin, S.-H.; Kim, Y.; Moon, S.-H. A review on recent developments of anion exchange membranes for fuel cells and redox flow batteries. *RSC Adv.* **2015**, *5*, 37206–37230. [[CrossRef](#)]
42. Parks, G.A. Aqueous Surface Chemistry of Oxides and Complex Oxide Minerals. In *Equilibrium Concepts in Natural Water Systems*; American Chemical Society: Washington, DC, USA, 1967; Volume 67, pp. 121–160.
43. Gupta, A.; Kumar, A.; Hegde, M.S.; Waghmare, U.V. Structure of Ce_{1-x}Sn_xO₂ and its relation to oxygen storage property from first-principles analysis. *J. Chem. Phys.* **2010**, *132*, 194702. [[CrossRef](#)]
44. Wang, L.; Fei, T.; Deng, J.; Lou, Z.; Wang, R.; Zhang, T. Synthesis of rattle-type SnO₂ structures with porous shells. *J. Mater. Chem.* **2012**, *22*, 18111–18114. [[CrossRef](#)]
45. Abbas, M.; Zhang, J.; Lin, K.; Chen, J. Fe₃O₄ nanocubes assembled on RGO nanosheets: Ultrasound induced in-situ and eco-friendly synthesis, characterization and their excellent catalytic performance for the production of liquid fuel in Fischer-tropsch synthesis. *Ultrason. Sonochem.* **2018**, *42*, 271–282. [[CrossRef](#)] [[PubMed](#)]
46. Ramesh, R.; Ashok, K.; Bhalero, G.M.; Ponnusamy, S.; Muthamizhchelvan, C. Synthesis and properties of α-Fe₂O₃ nanorods. *Cryst. Res. Technol.* **2010**, *45*, 965–968. [[CrossRef](#)]
47. Prashar, A.K.; Mayadevi, S.; Nandini Devi, R. Effect of particle size on selective hydrogenation of cinnamaldehyde by Pt encapsulated in mesoporous silica. *Catal. Commun.* **2012**, *28*, 42–46. [[CrossRef](#)]
48. Durndell, L.J.; Parlett, C.M.A.; Hondow, N.S.; Isaacs, M.A.; Wilson, K.; Lee, A.F. Selectivity control in Pt-catalyzed cinnamaldehyde hydrogenation. *Sci. Rep.* **2015**, *5*, 9425. [[CrossRef](#)] [[PubMed](#)]
49. Vriamont, C.; Haynes, T.; McCague-Murphy, E.; Pannetreau, F.; Riant, O.; Hermans, S. Covalently and non-covalently immobilized clusters onto nanocarbons as catalysts precursors for cinnamaldehyde selective hydrogenation. *J. Catal.* **2015**, *329*, 389–400. [[CrossRef](#)]
50. Handjani, S.; Marceau, E.; Blanchard, J.; Krafft, J.-M.; Che, M.; Mäki-Arvela, P.; Kumar, N.; Wärnå, J.; Murzin, D.Y. Influence of the support composition and acidity on the catalytic properties of mesoporous SBA-15, Al-SBA-15, and Al₂O₃-supported Pt catalysts for cinnamaldehyde hydrogenation. *J. Catal.* **2011**, *282*, 228–236. [[CrossRef](#)]

